Structural Properties of Prion Protein Protofibrils and Fibrils: An Experimental Assessment of Atomic Models†

Mari L. DeMarco,‡ Jay Silveira,§ Byron Caughey,§ and Valerie Daggett*,‡

Department of Medicinal Chemistry, Biomolecular Structure and Design Program, University of Washington, Seattle, Washington 98195-7610, and Laboratory of Persistent Viral Diseases, Rocky Mountain Laboratories, National Institute of Allergy and Infectious Diseases, National Institutes of Health, Hamilton, Montana 59840

Received June 26, 2006; Revised Manuscript Received October 3, 2006

ABSTRACT: Decades after the prion protein was implicated in transmissible spongiform encephalopathies, the structure of its toxic isoform and its mechanism of toxicity remain unknown. By gathering available experimental data, albeit low resolution, a few pieces of the prion puzzle can be put in place. Currently, there are two fundamentally different models of a prion protofibril. One has its building blocks derived from a molecular dynamics simulation of the prion protein under amyloidogenic conditions, termed the spiral model. The other model was constructed by threading a portion of the prion sequence through a β-helical structure from the Protein Data Bank. Here we compare and contrast these models with respect to all of the available experimental information, including electron micrographs, symmetries, secondary structure, oligomerization interfaces, enzymatic digestion, epitope exposure, and disaggregation profiles. Much of this information was not available when the two models were introduced. Overall, we find that the spiral model is consistent with all of the experimental results. In contrast, it is difficult to reconcile several of the experimental observables with the β-helix model. While the experimental constraints are of low resolution, in bringing together the previously disconnected experiments, we have developed a clearer picture of prion aggregates. Both the improved characterization of prion aggregates and the existing atomic models can be used to devise further experiments to better elucidate the misfolding pathway and the structure of prion protofibrils.

The term "prion" refers to a proteinacious infectious material that can transmit a trait (disease) in the absence of nucleic acid (*1*, *2*). The namesake of this type of non-Mendelian inheritance or infection strategy is the prion protein (PrP).[1] PrP can take on two identities: PrP^C, a monomeric partially structured protein containing primarily α-helices, and PrP^{Sc}, an aggregate-prone structure with primarily β-like extended secondary structure. By partially unfolding and then misfolding, PrP^C becomes PrP^{Sc}. While PrP^C is innocuous and thought to play a role in cell signaling (*3*) and/or copper metabolism (*4*), PrP^{Sc} can aggregate and cause neurodegeneration.

PrP^{Sc} is formed in a posttranslation process from PrP^C (*5*, *6*), involving partial unfolding of PrP^C and its subsequent misfolding at the surface of the plasma membrane and/or in the low-pH environment of the endocytic pathway (*6*−*8*). The misfolded protein, PrP^{Sc}, aggregates and forms amyloid fibrils and plaques, amorphous aggregates, and smaller aggregates or protofibrils (also referred to as soluble oligomers) (*9*−*12*). PrP^C can be completely digested by proteinase K, while the C-terminal residues ∼90−231 of PrP^{Sc} resist proteinase K digestion (which led to the nomenclature of PrP-sen and PrP-res for proteinase K sensitive and resistant forms, respectively) (*13*, *14*). Fourier transform infrared (FTIR) and circular dichroism (CD) spectroscopy experiments indicate a dramatic difference in the secondary structure between the two isoforms; PrP^C contains 47% α-helix and 3% β-structure, whereas PrP^{Sc} contains 17−30% α-helix and 43−54% extended structure; this range is partially due to the multiple forms and lengths of PrP^{Sc} (*14*−*16*). High-resolution structural information for PrP^{Sc} aggregates is nonexistent.

There is increasing evidence that small aggregates (known as protofibrils or oligomers), not fibrils, are the primary cytotoxic species in amyloid diseases (*17*−*21*). Furthermore, recent studies indicate that the most infectious particle per unit PrP has an average mass equivalent to a 14−28-mer with the minimal infectious unit being larger than a 5-mer (*22*). For both prion and other amyloid diseases, preventing or disrupting protofibril formation appears to be necessary for disease prevention. Prevention or disaggregation of mature (amorphous or amyloid) aggregates may lead to increased concentration of the toxic protofibrils (*23*). Thus, structural insights into protofibril formation are of central importance in the pursuit of therapeutic targets.

Currently, two fundamentally different protofibril models of PrP^{Sc} have been proposed. One PrP^{Sc}-like structure was

† We gratefully acknowledge support from the National Institutes of Health (GM-50789 to V.D. and a National Research Service Award T32 GM-07750 to M.L.D.) and a Hope Barnes Fellowship to M.L.D.

* Corresponding author: e-mail, daggett@u.washington.edu; phone, 206-685-7420; fax, 206-685-3252.

‡ University of Washington.

§ National Institute of Allergy and Infectious Diseases, NIH.

[1] Abbreviations: PrP, prion protein; PrP^C, cellular prion protein; PrP^{Sc}, scrapie prion protein; MD, molecular dynamics; EM, electron microscopy.

10.1021/bi0612723 CCC: $33.50
Published on Web 12/01/2006

derived from a molecular dynamics (MD) simulation under amyloidogenic conditions in which the conversion process is observed directly (*24*). The other was modeled by threading a portion of the prion sequence through a known β-helix fold (*11*, *25*). The first model has a spiraling core of extended sheets formed by parallel and antiparallel extended strands, which we call the spiral model. The other model has a core of left-handed β-helices (parallel β-strands), with subunits arranged on the basis of the left-handed β-helix of the C-terminal domain *N*-acetylglucosamine-1-phosphate uridyltransferase (*26*): the β-helix model. In the present study, these two protofibril models are evaluated for consistency with pertinent experimental data.

METHODS

All sequence numbers are reported relative to the Syrian hamster (SHa) sequence unless otherwise noted. For example, the β-helix protofibril contains residues 89−227 of the mouse/human PrP chimera and is reported as 90−228 in the SHa numbering scheme.

The minimal protofibril diameter refers to the minimal cross-sectional distance of a protofibril taken perpendicular to the fiber axis. The maximal diameter refers to the diameter of a circle, lying perpendicular to the fiber axis, required to encompass all atoms of interest (i.e., protein only) of a protofibril. Hydrogen atoms were not considered in these measurements.

A triantennary glycoform scaffold, common to PrP^C and PrP^{Sc} (*27*, *28*), was N-linked to Asn-181 and Asn-197 of both models and oriented to best accommodate the tight packing, based on the electron microscopy (EM) unit cell, between neighboring protofibrils (Figure 1).

The XtalView software package (*29*) was used to pack neighboring protofibrils in an arrangement consistent with the unit cell and symmetry constraints (*11*). The unit cell dimensions used were $a = b = 69$ Å, and protofibrils were rotated (in the *xy* plane) to best accommodate packing restraints.

The procedure for the partial disaggregation and analysis of PrP-res has been described previously (*22*).

RESULTS AND DISCUSSION

Origin of Models. The β-helix model originates from a survey of all-β folds looking for structures that had a diameter of <50 Å and formed β-sheets with accessible edges. From this search a left-handed β-helix was selected (*25*). In the spiral model, the subunit is derived from an all-atom, explicit solvent MD simulation (*24*). Beginning with the NMR structure of PrP^C, a simulation under amyloidogenic conditions (low pH) was performed at 25 °C. A misfolded ensemble formed during the simulation, and from this ensemble a representative structure (unmodified from the simulation coordinates) was chosen to model aggregates. Similar building blocks have been obtained in various independent simulations, and these simulations demonstrate the effect of sequence on the structure of the misfolded species (*30*−*32*). The advantage of this approach is that the structural scaffold is not chosen arbitrarily; instead, one has a specific and realistic pathway for the conversion process leading to oligomerization.

Dimensions. Both models were developed to model PrP^{Sc} protofibrils, particularly targeting the dimensions of a small

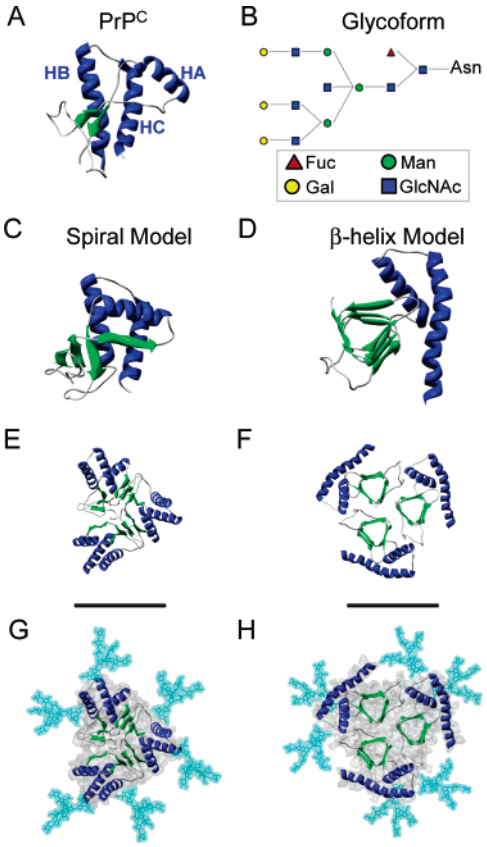

FIGURE 1: Monomeric and aggregate PrP structure. (A) PrP^C NMR structure. (B) The biologically relevant PrP glycans attached to each model [Fuc, L-fucose; Gal, D-galactose; GlcNAc, *N*-acetyl-D-glucosamine; Man, D-mannose]. (C) Spiral model, a PrP^{Sc}-like species from MD at low pH. (D) β-Helix model, derived by threading the PrP sequence through a known β-helix fold. A trimeric representation of (E) the spiral model (*24*) and (F) the β-helix model [coordinates provided by C. Govaerts (*11*)]. (G) The spiral model and (H) the β-helix model with the protein-only portion highlighted (gray, space-filling) and biologically relevant glycans (cyan, space-filling) attached to the appropriate glycosylation sites. Images E−H are on the same scale (bar = 50 Å).

aggregate studied by EM (*11*). In this EM study, PrP protofibrils fit within a 69 × 69 Å unit cell, allowing for a cross-sectional diameter (perpendicular to the fiber axis) of less than 69 Å for the protein portion of the protofibril. The minimum and maximum diameters, excluding glycans, of the spiral model are 58 and 67 Å, and those of the helix model are 68 and 90 Å, respectively (Figure 1). Although the maximal diameter of the β-helix model is larger than the diameter constraint by EM, the grooves along the surface of the protofibrils allow protein-only protofibrils to fit together within the 69 Å constraints.

The Asn-linked glycans lie on the periphery of each protofibril, as evidenced by EM images (*11*). While the glycans attached to the protein are flexible, they are almost as large in volume as the protein itself, and therefore their size alone presents challenges for modeling compact aggregates. PrP^C can convert to PrP^{Sc} with or without the glycans present, but in the constructs used for the EM data they were present and therefore they must be included in the models.

In the β-helix model reported by Govaerts et al., five sugar residue glycans were attached at both glycosylation sites (*25*).

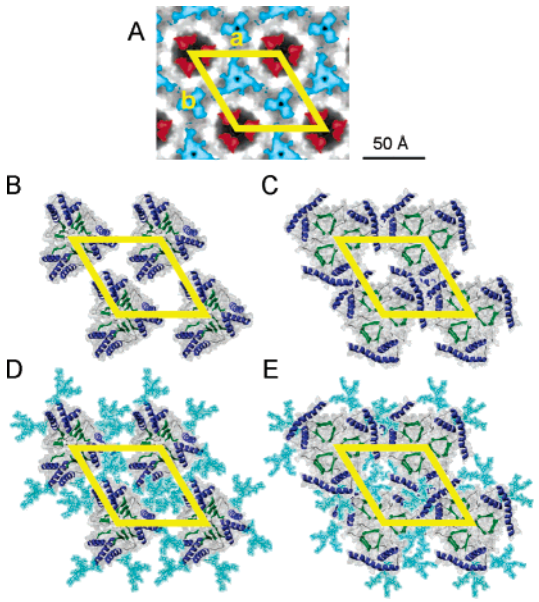

FIGURE 2: Dimensional constraints on protofibril size. (A) The unit cell (yellow) of the prion protofibrils from EM (*25*) (where $a = b = 69$ Å). Location of internal residues 142−177 (red) and glycans (cyan) are illustrated. Using XtalView, trimers from the (B) spiral model and (C) β-helix model were packed on the edges of the unit cell. (D, E) Biologically relevant glycans (cyan) were added to each model and arranged to minimize clashes with protein atoms from neighboring protofibrils. (D) There is sufficient void volume to add biologically relevant glycans, within the constraints of the unit cell, in the spiral model. (E) The β-helix model with biologically relevant glycans does not fit within the constraints of the unit cell. All images are on the same scale (bar = 50 Å).

These glycans are much smaller than the natural glycans, as the predominant glycans on PrP have ~8−20 sugar residues at each glycosylation site (*27*, *28*). Over 400 different PrP glycoforms have been identified, and a representative glycoform of moderate size (13 sugar residues) and complexity (triantennary) was selected for the spiral model (*24*). To compare the dimensions of the models under similar and, more importantly, biologically relevant conditions, both models were given the same triantennary glycans with 13 sugar residues each and oriented to best accommodate the tight packing between neighboring protofibrils (Figure 1).

Using trimers of each model, a layer of the idealized protofibril was constructed for each model using XtalView (*29*) to demonstrate the dimensional constraints of the EM data, $a = b = 69$ Å and space groups $P3_1$ for the spiral model and $P3$ for the β-helix model (Figure 2). In Figure 2 four trimeric protofibrils of only protein atoms of each model are packed according to the EM unit cell. Of the two models, only the spiral model has enough void volume to accommodate biologically relevant glycans (Figure 2D,E). Additionally, in the spiral model, there is ample volume to accommodate multiple conformations of the glycans. In the β-helix model there is insufficient space surrounding the protofibrils for even minimal 13-residue PrP glycans (Figure 2E), and thus, the β-helix model does not agree with the experimental EM data it was reported to fit (*11*, *25*). To accommodate the unit cell dimensions, the glycans in the β-helix model could be positioned above and below the two-dimensional EM plane. However, such a model would be inconsistent with the position of the glycans in the EM images (*11*, *25*) and may limit the maximum size of the β-helix protofibril to a hexamer as the glycans would block the proposed oligomerization edges.

One of the attractive aspects of the β-helix model is that it includes nearly all of the residues (residues 90−228) in the PrP 27−30 construct (residues 90−231). While the full-length PrP construct comprises residues 23−231, upon conversion, residues 23−89 remain accessible and in a similar conformation to PrP^C (based on antibody binding studies) (*33*). These N-terminal residues are not involved in fibril formation nor are they protected from proteinase K cleavage (*34*); as such, the maximal construct believed to be involved in fibril formation comprises residues 90−231, which is denoted PrP 27−30. The subunits of the spiral model begin at residue 109 [corresponding to the NMR structure of $SHaPrP^C$ used for the original misfolding simulation (*24*)] and end at residue 219. The C-terminal residues are trivial to model in, as there is experimental evidence to guide us. This model is shown in a previous work (*24*), and the C-terminal extension does not add to the diameter of the protofibril. The N-terminal residues can be modeled in as a continuation of the existing β-sheet, resulting in a modest increase in the minimal diameter (from 57 to 58 Å), or packed against the existing sheet with no increase in diameter. Thus, these residues can be modeled onto the existing spiral protofibril without violating the experimental constraints.

Aggregate Formation. The driving force and stabilization of aggregation are believed to be exposure of hydrophobic surfaces (*35*, *36*), electrostatic interactions (*36*, *37*), aromatic stacking (*37*, *38*), and particularly main chain−main chain interactions (*35*, *39*−*41*). It is likely a combination of these interactions that make amyloid fibrils, prion amyloid fibrils in particular, so stable. In designing models of preamyloid aggregates, it seems reasonable to assume that even the early aggregates incorporate some of the interactions of their more mature counterparts.

In the spiral model, each subunit has two oligomerization edges (extended strands) that allow growth in either direction along the fiber axis. Subunits bind through hydrophobic extended strands, connecting neighboring subunits by a four-stranded extended sheet. All oligomerization sites are identical; each subunit adds to the protofibril in the same way. Aggregation and stabilization can be explained by hydrophobic packing and by hydrogen bonding across the sheet (Figure 3).

In the β-helix model there is a distinct difference in aggregation between subunits within a trimeric disk and between these disks. Interactions between subunits that lie in the same plane perpendicular to the fiber axis (like slices of a pizza), or intradisk interactions, are nonspecific side chain−side chain interactions. This is in contrast to the PDB structure (1G97, C-terminal domain *N*-acetylglucosamine-1-phosphate uridyltransferase) it is modeled after, where specific side chain interactions, π-stacking and hydrophobic clusters, hold the subunits of the trimer together. The reasoning for interdisk aggregation (aggregation between trimeric disks or growth beyond a trimer) in the β-helix model is unclear. The paired edges between the C-terminal surface of one β-helix and the N-terminal surface of the subunit below it are not complementary. Only one of the three end strands has the possibility of forming a strand-to-strand interface (interface A, Figure 3B). The other two edges

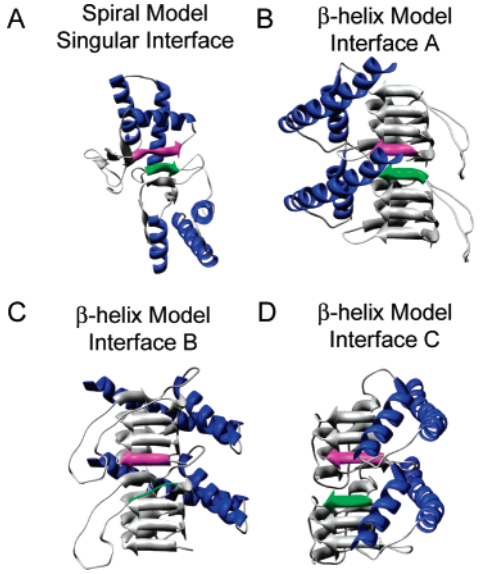

FIGURE 3: Aggregation interfaces. (A) Hydrophobic packing and backbone hydrogen bonds hold subunits together in the spiral model. (B) Noncomplementing surfaces and steric hindrance prevent H-bonding between subunits in the β-helix model. The edge strands of adjacent subunits that form the oligomerization interface are colored magenta and green.

are strand-to-unstructured loop (interface B, Figure 3B) and strand-to-solvent (interface C, Figure 3D) interfaces. β-Helical proteins in the PDB use irregular outer surfaces such as this to *prevent* aggregation (*42*). Besides the irregular outer edges of the β-helix, the α-helices and the first glycan prevent tight packing between subunits. The distances between the three aggregation edges (shown in Figure 3B−D) are approximately 6.5, 10.7, and 10.8 Å (measured by averaging Cα−Cα distances between adjacent strands). For hydrogen bonding to occur, the distance between Cα atoms in parallel strands should be ∼4.7 Å. When the two strands of interface "A" are brought into H-bonding range, clashes between subunits occur. While main chain interactions are known to play a central role in aggregation and amyloid formation (*35*, *39*−*41*), they are only present within individual subunits of the β-helix. There are minimal intra- and interdisk main chain−main chain interactions in the β-helix model, and as such, it predicts that these interactions are unimportant in aggregation.

The β-helix and spiral models predict the generation of distinct fragmentation patterns upon fibril disassembly. Disassembly of β-helix-based fibrils would be expected to involve the preferential removal of trimeric disks because the actual protofibrillar disks (whether trimeric or hexameric) are stable enough to be seen as discrete units by EM (*11*, *25*), and as detailed above, it is much easier to identify plausible chemical forces for strong intradisk interactions than for interdisk interactions. Thus, incomplete dissociation of β-helix-based fibrils would be expected to generate a pattern of fragments that differ in mass by ∼75 kDa, i.e., the average mass of a trimer. However, small oligomers generated by various treatments of hamster 263K PrP 27−30 aggregates give ladders of bands in high-porosity PAGE gels that differ sequentially by ∼25 kDa, i.e., the equivalent of a monomer, with no evidence of greater abundance or stability of trimeric and hexameric protofilaments at 75 and 150 kDa, respectively (Figure 4). To generate the bands,

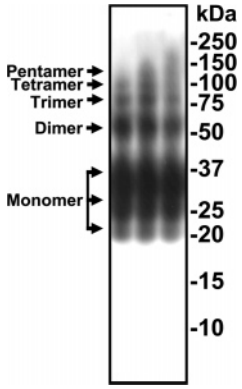

FIGURE 4: Fragmentation pattern of PrP 27−30. Hamster PrP 27−30 (263K strain) was partially dissociated, fractionated by size using flow field−flow fractionation (Fl-FFF), electrophoresed without further denaturation using a 10% PAGE gel, and then analyzed by immunoblotting using anti-PrP monoclonal antibody 3F4 as described previously (*22*). Three sequential early Fl-FFF fractions are shown containing monomer bands (resolved into three glycoform groups) and small oligomer bands (in which the glycoforms are not resolved) as designated. Positions of molecular mass markers are designated on the right.

hamster PrP 27−30 (263K strain) was partially dissociated, fractionated by size using flow field fractionation, electrophoresed without further denaturation using a 10% PAGE gel, and then analyzed by immunoblotting using anti-PrP monoclonal antibody 3F4 as described previously (*22*). Three sequential early flow field fractions are shown containing monomer bands (resolved into three glycoforms) and small oligomer bands (in which the glycoforms are not resolved). These results are incompatible with the β-helix model but are fully consistent with the spiral model in which protofibrils are assembled and disassembled sequentially in monomeric, rather than trimeric, units.

Symmetry. Prion protofibrils have been estimated to have either 3- or 6-fold symmetry (*11*). The β-helix protofibril has 3-fold symmetry ($P3$), and the spiral protofibril has a right-handed 3-fold screw axis ($P3_1$). In three dimensions the differences in symmetry of the models are evident, yet in two dimensions (*x*- and *y*-axis) $P3$ is indistinguishable from $P3_1$. Since only one experiment provides information on protofibril symmetry, more are needed to validate this result; currently however, both models can account for the experimentally observed two-dimensional 3-fold symmetry.

In EM images the 3-fold symmetry can be observed in the center of the protofibril (Figure 5). To locate residues 142−177, a subtraction map of the EM image of the internal deletion construct $PrP^{Sc}106$ (residues 90−231, Δ142−177) and that of PrP 27−30 (residues ∼90−231) was constructed (*11*, *25*). Statistically significant differences between the maps were superimposed on a refined map and colored red (as seen in Figure 5A, taken from ref *25*). Residues 141−176 were colored accordingly on the models (Figure 5B,C). The β-helix model predicts that residues 142−177 are spread relatively equally over the interior of the fibril. The spiral model predicts that residues 142−177 are not found in the center of the fibril but in a ring around the center of the protofibril axis with HA creating high-density areas, possibly discernible by EM (Figure 5; all images are on the same scale).

The EM images predict that deletion of the 142−177 region results in protofibrils of similar size and morphology

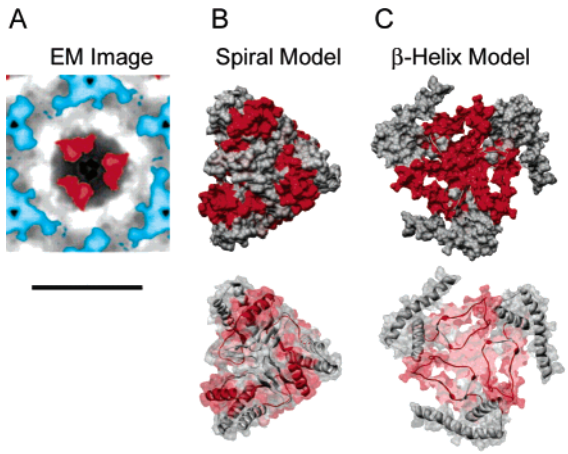

FIGURE 5: Symmetry of model protofibrils. (A) EM image with location of residues 142−177 colored in red and glycans in cyan (from ref *24*). (B, C) Space-filling models (excluding hydrogens) of protein-only slices of (B) the spiral model and (C) the β-helix model. All protein images are on the same scale (bar = 50 Å). The EM image is slightly smaller than the protein images.

to PrP 27−30 protofibrils. In the spiral model, deletion of these residues leaves the original scaffold (oligomerization sites), with a slight reduction in diameter. In the β-helix model, deletion of residues 142−177 results in the loss of a rung of the β-helix, leaving the diameter unchanged but increasing the already troublesome interdisk gap.

X-ray fiber diffraction experiments also provide insight into how subunits are arranged in the aggregates, more specifically, the arrangement of all, or part, of the extended structure, at least for amyloid fibrils (*40*, *43*). Fiber diffraction (*40*, *43*, *44*) and X-ray crystallographic experiments (*45*) indicate that the amyloid fibril structure is not β-helix. Similarly, the orientation of the sheets in the spiral model precludes the spiral model from reproducing the reflections of amyloid. Protofibrils are more soluble, more infectious, smaller, and less ordered than their amyloid counterparts (*22*); therefore, we do not expect that protofibrillar species would generate the same diffraction patterns as amyloid. Further conformational rearrangement is expected in the protofibril to fibril transition. In the spiral model, two hinge motions per subunit can bring the sheets into amyloid-like arrangement. In the β-helix model refolding of the β-helix back into extended sheets could reproduce amyloid-like fiber diffraction properties. In the transition from protofibril → amyloid fibril we consider modest rearrangement/repacking of the existing structure to be more realistic than the unraveling and refolding of the N-terminal portion of the protein from a β-helix (already a significant conformational change from the native state) back into a structure with extended sheets.

Secondary and Tertiary Structure. One way to distinguish PrP^C from PrP^{Sc} is to measure the secondary structure content of the sample. In the $PrP^C \rightarrow PrP^{Sc}$ conversion the percentage of β-structure increases dramatically from 3% to 43−54% and α-helix decreases from 43−47% to 17−30% (*14*−*16*). We calculated the amount of secondary structure in both models to compare with the experimental data (Table 1). The PrP constructs used in the theoretical models and those found in the experimental fibrils are of differing lengths; PrP in experimental fibrils composed of PrP 27−30 have varying lengths (the "27−30" referring to the subunit mass of the fibrils being in the range of 27−30 kDa) and contain approximately 142 residues (residues 90−231), the spiral model has 111 residues (residues 109−219), and the β-helix model has 139 (residues 90−228). The number of residues in either α or extended conformation (repeating structure only; see Table 1) was calculated for the spiral model by averaging over the PrP^{Sc} ensemble from simulation, 6−20 ns, and for the β-helix model the number of residues was counted directly from the PDB HELIX/SHEET header records provided by C. Govaerts (*25*). Compared to the 43−54% β-sheet in PrP 27−30, both the β-helix model and the spiral model fall short with 29% and 30% extended structure, respectively (Table 1). By examining the region where the constructs overlap, residues 109−219, the β-helix model has 27% β-structure compared to the 30% in the spiral model (Table 1). For the 109−219 construct, both models have approximately 10-fold greater levels of extended structure than PrP^C. To compare both models to the experimental 90−231 construct, residues 90−108 were modeled onto the spiral model (since the additional β-structure at the N-terminus is modeled in and has not been acquired directly through MD simulations, it is only discussed in this section so that a realistic experimental comparison can be made). The spiral model falls within the experimental range (43−54%), with 46% extended structure, while the β-helix model remains at 30% extended structure. To be in agreement with the CD and FTIR secondary structure data, the β-helix model must undergo another conformational change. The spiral model, as presented, accommodates the hallmark feature of conversion: the observed increase in extended structure.

The amount of repeating α-helix structure in each model, 33% in the spiral model and 32% in the β-helix model, is close to the experimental range, 17−30%, for PrP 27−30 fibrils (Table 1), as expected for models that retain most of the native helices. In MD simulations, the N-terminus of HB unwinds, and in the β-helix model the same region was modeled to be unstructured. The disulfide bond, which is maintained upon fibril formation (*46*, *47*), is present in both models.

Helix A. One major difference between the models is that helix A (HA) is largely conserved in the spiral model and changes conformation (it is part of the β-helix and an unstructured loop) in the β-helix model (Figure 1). While HA was once hypothesized to be unstable and likely to unfold during the initial steps in misfolding (*48*), recent experiments exploring the stability, helicity, and amyloidogenicity of HA have demonstrated the opposite. HA, as a peptide, has no propensity to form amyloid and, when added to amyloidogenic sequences, slows fibril formation (*49*). HA also has a high helical propensity under a variety of conditions (*50*), despite its atypical hydrophilic sequence. Even engineered mutants of PrP^C designed to destabilize HA did not reduce the helicity of HA nor destabilize PrP^C (*24*, *51*). Furthermore, Watzlawik and co-workers (*52*) have shown that HA (residues 144−154) is not converted to β-structure by comparing PrP fragments 23−144 and 23−159, which correspond to the human disease related 145 and 160 stop mutants. Interestingly, the longer fragment aggregates more rapidly, which given the lack of conversion of HA is probably due to the added stability of the residues C-terminal to HA compensating for the lack of S2. While it is possible that HA unfolds and converts to extended structure at some point during fibril formation, it is not required to

Table 1: Secondary Structure of Experimental Fibrils and Protofibril Models

	construct				secondary structure[c]			
	aggregate type	origin	residues[a]	no. of residues	no. of α residues	no. of β residues	% α	% β
experiment	fibril	SHa brain/PK	~90−231[b]	~142[b]	24−43[d]	61−77[d]	17−30[e]	43−54[e]
β-helix	protofibril	modeling	90−228	139	45[f]	40[f]	32	29
spiral	protofibril	MD/modeling	109−219	111	37[g]	33[g]	33	30
β-helix fragment	protofibril	modeling	109−219	111	36[f]	30[f]	32	27

[a] SHaPrP numbering. [b] Variable length due to proteinase K digestion. [c] Amount of repeating secondary structure (i.e., three or more consecutive residues). [d] Calculated from CD and IR percent secondary structure (using a 142-residue construct). [e] Estimates from CD and IR experiments (*14*−*16*). [f] The number of residues in the α-helix and β-structure conformation is from the β-helix model HELIX/SHEET PDB header information provided by C. Govaerts. [g] Secondary structure values averaged over misfolded ensemble from MD simulation (6−20 ns) and calculated by ϕ, ψ analysis (*67*) and hydrogen bond networks.

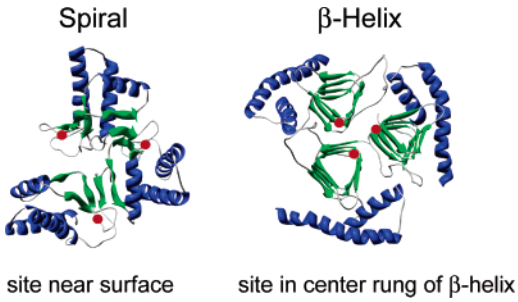

FIGURE 6: Minor proteinase K cleavage site (red). Small circles mark each Gly-127 cleavage site.

accommodate the amount of extended structure observed in PrP^{Sc} by CD and FTIR. As demonstrated by the spiral model, conversion of N-terminal regions, excluding HA, produces the amount of extended structure in accordance with the experimental range. In addition, according to antibody binding studies (see the Epitope Mapping section below for details), the bulk of HA, HB, and HC is preserved in prion fibrils. Focusing on HA, this region lies at or near the surface of fibrils, readily accessible to antibodies (*53*). In summary, experimental evidence indicates that HA is folded, or at least largely folded, and located near the surface of the fibril. The spiral model shares these properties; however, in the β-helix model HA is completely unfolded and buried within the core of the protofibril.

Amyloidogenic and Amyloid-Inhibiting Sequences. As shown for HA, in addition to the amount of structure, the location of structure is useful for model validation. While many peptides derived from the prion sequence can form amyloid, assessing amyloidogenicity and the inhibitory properties of these peptides has resulted in the identification of sequences critical to misfolding and aggregation. According to turbidimetric aggregation assays of overlapping peptides from the human PrP sequence, the region between S1 and HA in PrP^{C} was identified as having a high aggregation propensity (*49*). This region corresponds to the E4 strand in the spiral model, a key strand in the aggregation process, as it forms an oligomerization site. This region forms part of a strand−turn in the β-helix model and is involved in neither intra- nor interdisk interactions. The proposed ability of this region to initiate fibril formation (*49*) is supported by the spiral model and is contradicted by the β-helix model.

In measuring the ability of PrP-derived peptides to inhibit conversion, two critical regions, residues 113−120 and 129−141, were identified (*54*). For maximal inhibition, PrP-derived peptides required residues 113−120. Additionally residues 129−141 were important for inhibition, as peptides containing both sequences (109−141 and 113−141) were significantly more inhibitory than those containing only the 113−120 sequence. Consistent with the peptide study, experiments with N-terminally truncated versions of the protein found that residues within 105−120 are required for conversion (*55*). Assuming the peptides bind to the protein in the same manner as the corresponding sequences in the models, we can make some interesting observations about the mechanism of inhibition. The two inhibitory sequences overlap with the oligomerization interface in the spiral model, which forms through strand E1 (residues 116−119) of one subunit and E4 (residues 135−140) of the adjacent subunit. The spiral model readily accounts for the strong inhibitory properties of the peptides in that they directly block one (for peptides containing the 113−120 region) or both (for peptides that span both critical regions) of the oligomerization edges in a growing protofibril (*24*). In the β-helix model both of these critical regions reside within the core of the β-helix; they are located at neither inter- or intradisk oligomerization sites. In order to make a valid comparison between the models and experiment, we must also examine PrP-derived peptides that span the proposed interdisk oligomerization sites in the β-helix model (Figure 3). Fortunately, PrP-derived peptides that overlap with the N- and C-terminal oligomerization edges of the β-helix, peptides 89−103 and 139−170, have been studied (*54*). The 89−103 peptide, which overlaps with the N-terminal oligomerization edge of the β-helix, is only weakly inhibitory at very high concentrations; the 139−170 peptide, which covers all potential C-terminal oligomerization edges of the β-helix model, had no inhibitory effect.

In the β-helix model, weakly inhibitory sequences reside at the oligomerization interfaces, a noninhibitory peptide corresponds to an oligomerization interface, and the strongly inhibitory sequences are uninvolved in oligomerization, all of which is counterintuitive. The spiral model accounts for, and provides a reasonable mechanism for, the amyloidogenic and inhibitory properties of PrP-derived peptides.

Enzymatic Cleavage Sites. A common PrP^{Sc} identification and purification method, treatment of fibrils with proteinase K, can be used to identify exposed residues in PrP^{Sc} fibrils. The major cleavage site of proteinase K is at Gly-90; however, there are minor cleavage sites, one of which, Gly-127, is within the overlapping sequence of the two models (*56*). Since PrP^{Sc} fibrils are cleaved at Gly-127 by proteinase K without the use of denaturants, it is improbable that this residue is in the core of the fibril. It is reasonable to expect that Gly-127 be near the fibril surface. The location of Gly-

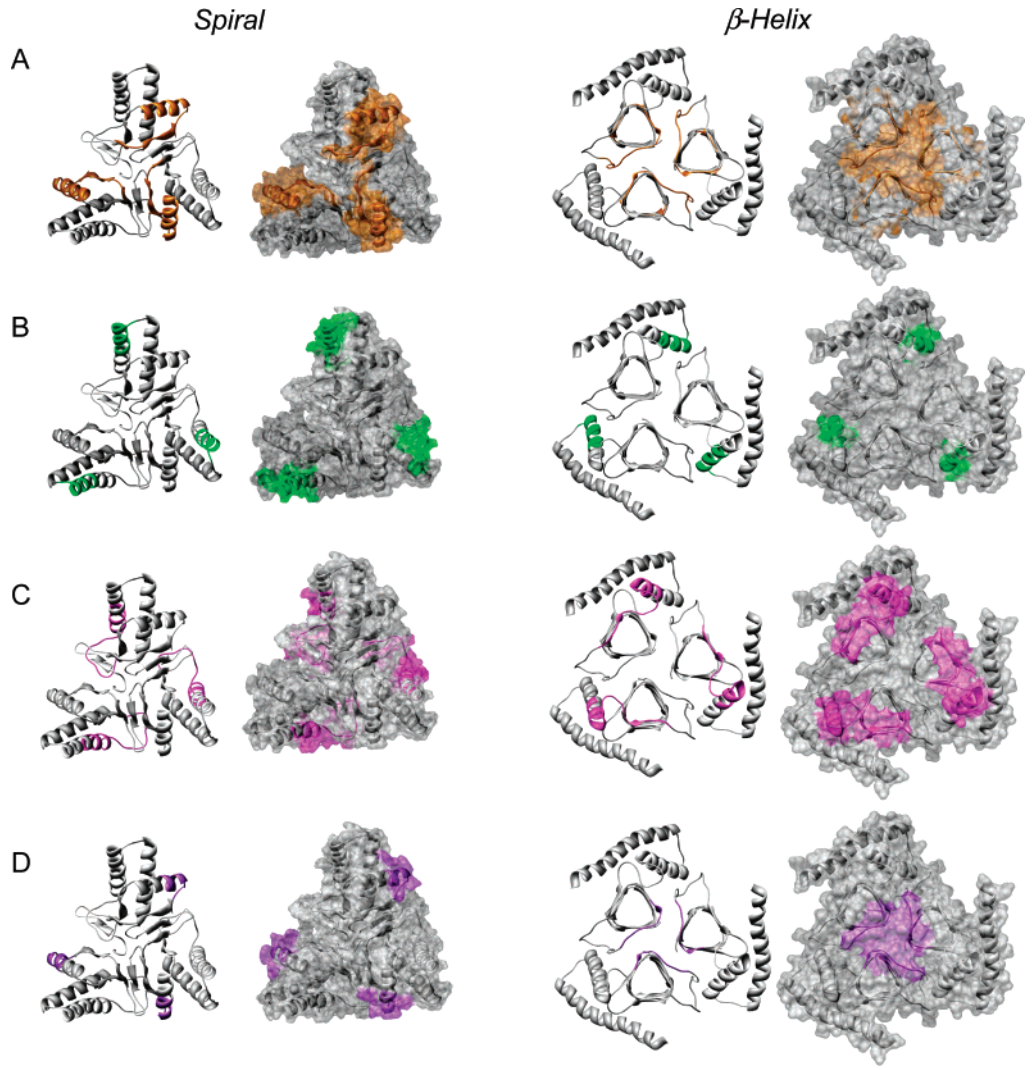

FIGURE 7: Mapping known epitopes onto the spiral and β-helix models. A cross-section perpendicular to the fiber axis of each protofibril is shown (trimeric representation); for epitopes to be accessible they must be on the edge of the image. (A) A primarily PrP^C-selective mouse antibody (also able to clear PrP^{Sc}) binds residues 136−156 (colored orange), (B) ovine nonselective antibody (binds PrP^C and PrP^{Sc}) binds residues 185−196 (colored green), (C) human nonselective PrP^C and PrP^{Sc} antibody binds residues 165−185 (colored magenta), and (D) human nonselective PrP^C and PrP^{Sc} antibody binds residues 141−149 (colored purple). Space-filling models (excluding hydrogens) are shown beside their corresponding ribbon diagram.

127 in the two protofibril models is shown in Figure 6. Gly-127 in the β-helix model is buried in the protofibril and unlikely to be cleaved by the enzyme. On the other hand, Gly-127 is found near the surface of the protofibril in the spiral model.

Epitope Mapping. A powerful method for identifying areas of conformational diversity and similarity between PrP^C and PrP^{Sc} is through antibody mapping studies (*57*). Antibody mapping has been used to explore the surface of PrP^{Sc} fibrils (not protofibrils); therefore, comparisons between antibody binding data and model protofibril structures cannot be used as definitive experimental checks. However, these studies identify regions that may or may not change during the course of conversion. A PrP^C selective antibody, D18, not only blocks conversion of PrP^C to PrP^{Sc} but, through an unknown mechanism, also reverses PrP^{Sc} formation (*58*, *59*). This antibody binds to residues within 132−156 of the sequence, a region that encloses HA (*60*). In the spiral model, this region is essentially unchanged upon conversion (Figure 7A). However, upon oligomerization, neighboring PrP^{Sc} subunits block portions of this epitope, leaving only a single complete epitope exposed at the trailing edge of the protofibril. Since the structure of the 132−156 region remains unchanged and the epitope remains exposed at one of the oligomerization edges, the D18 antibody may be able to clear PrP^{Sc} by interacting with the exposed and unchanged epitope.

The plausible structure and location of the 132−156 region in PrP fibrils have been further elucidated by recent studies using antibodies to probe the surface of single PrP fibrils. Using in vitro generated recombinant PrP fibrils untreated with proteinase K, the binding of the D18 antibody and another antibody binding to 136−158 to fibrils was assessed (*53*). Two different fibril morphologies were found, one in which antibodies bound to the 136−158 epitope and another where they did not bind to the 132−156 (D18) epitope. Under mildly denaturing conditions, binding to the 132−156 epitope was recovered. Fluorescence studies indicated that the fibril did not undergo significant unfolding to expose this epitope and that the epitope was exposed in a uniform manner along the surface of the fibril. These results suggest that the 132−156 region is (1) at or close to the surface fibrils, (2) in a location that (if partially buried) allows for

Table 2: Summary of Experimental Comparisons

experiment	model in agreement? spiral	*β-helix*	ref
electron microscopy			*11, 25*
unit cell	yes	no	
location and fit of glycans	yes	no	
location of deletion residues	yes	yes	
symmetry	yes	yes	
disaggregation profiles			*22*
monomeric building blocks	yes	no	
X-ray fiber diffraction of fibril	no	no	*43*
CD and IR spectra			*14−16*
β-structure	yes[a]	no[b]	
α-helix	yes	yes	
conformation and stability of helix A			*50−52*
HA is stable as helix	yes	no	
immunoconformational assay			*53*
HA at least partially folded	yes	no	
HA near surface	yes	no	
turbidimetric analysis			*49*
amyloidogenic sequences correspond to critical aggregation sites	yes	no	
conversion assays and inhibitors			*54*
113−120, 129−141 inhibitors	yes	no	
109−141, 113−141 inhibitors	yes	no	
139−170 noninhibitory	yes	no	
proteinase K digestion			*56*
Gly-127	yes	no	
epitope mapping			
136−152	yes	no	*53, 58, 59*
142−148, 162−170, 214−226	yes	no	*62*
219−232, 225−231	yes	yes	*60, 63*
185−196	yes	no	*64*
141−149	yes	no	*61*
165−185	yes	no	*61*

[a] The 90−230 spiral model is consistent with the CD and IR data for PrP 27−30. [b] The *β*-helix model has 29% *β*-structure and the experimental range is 43−54%.

exposure without significant disruption of the fibril, and (3) from previous studies is in a similar conformation to PrPC (*58*, *59*, *61*). All of these characteristics further reinforce the plausibility of the spiral model and negate the *β*-helix model.

In contrast, the D18 epitope changes conformation in the *β*-helix model (Figure 7A). While this region is exposed at one face of the protofibril, it has drastically altered secondary and tertiary structure, which could account for the lack of observable D18 antibody binding. Thus, both models account for the lack of D18 antibody binding, and the spiral model also provides a possible explanation for PrP^{Sc} clearance with the antibody, which suggests that there is an interaction between the antibody and PrP^{Sc}. Furthermore, the spiral model can account for the behavior of the D18 epitope under mildly denaturing conditions.

In the case of monoclonal antibody I5B3, it is PrP^{Sc}-selective as it can precipitate bovine, murine, and human PrP^{Sc} by binding to the discontinuous epitope comprised of residues 142−148, 162−170, and 214−226 (*62*). The residues comprising this discontinuous epitope come together in the spiral model to form a continuous and accessible surface (*24*). The *β*-helix model is not in agreement, as residues 142−148 (contained in the D18 epitope) are buried in the protofibril.

Nonselective antibodies, while not discriminating between monomeric (PrP^{C}) and aggregated species (PrP^{Sc}), can also be useful for model verification. Although these studies are typically done using PrP^{Sc} fibrils, it seems reasonable to assume that regions in PrP^{C} that are structurally conserved in PrP^{Sc} fibrils are likely to be conserved in the intermediate protofibrils. Examples of such nonselective antibodies include antibodies that bind to the C-terminal region of HC, mapping to residues 219−232 (*63*) and 225−231 (*60*). Both models conserve the HC helix (Figure 1). The spiral model is truncated at 219, and the *β*-helix model is truncated at 226. By modeling in the appropriate residues, both models easily accommodate PrP^{C}-like structure and accessibility in this region.

Another nonselective antibody is the OvPrP antibody whose epitope is found within residues 185−196 (residues 188−199 in Ov numbering) (*64*). The corresponding region on the two models is colored in green in Figure 7B. Both models have native-like structure in this region. In the spiral model this epitope is accessible to antibodies, consistent with experiment. In contrast, in the *β*-helix model, this region is buried, which is inconsistent with experiment.

Two monoclonal antibodies, SA65 and SA21, raised against rec-HuPrP in $Prnp^{0/0}$ mice were found to bind both PrP^{C} and PrP^{Sc} from humans with sporadic CJD, sheep and goats with scrapie, and cattle with BSE (*61*). The monoclonal antibodies were mapped to residues 141−149 and 165−185, and these epitopes are shown on the protofibril models in Figure 7C,D, respectively. In the spiral model both epitopes are accessible and in a similar conformation to PrP^{C}. In disagreement with this experimental observable, the *β*-helix model has both epitopes buried in the center of the protofibril in altered conformations from PrP^{C}.

In vivo, PrP^{Sc} has the peculiar property of not eliciting an immune response in the host, and generation, in the laboratory, of PrP^{Sc}-selective antibodies has been limited (only two reported cases) (*62*, *65*). Since PrP^{C} and PrP^{Sc} have the same covalent structure, the host immune system must recognize a distinct conformational epitope, and either there are few such epitopes (the exposed surfaces of PrP^{Sc} subunits in aggregates are similar in PrP^{C}) and/or the glycans limit the accessibility of antibodies to the protein surface. The latter assumption tends to be negated by the multitude of antibodies that bind to PrP^{Sc}, which are, unfortunately, also able to bind to PrP^{C}. Thus, the inability of both scientists and the host immune system to produce antibodies against PrP^{Sc} may be representing the similar outward appearance of subunits of PrP^{Sc} protofibrils or fibrils, and of PrP^{C}.

CONCLUSIONS

Until high-resolution structures of the infectious prion isoform are available, modeling can be a useful tool for transforming low-resolution data, from a variety of sources, into atomistic models. But modeling structures based on few experiments, and thus very few constraints, can lead to unrealistic structures. Developing a large set of constraints helps not only in the building process but also in the validation process.

In the case of the prion protein, only the spiral model (*24*) is consistent with a wide variety of experimental data (Table 2). The *β*-helical model (*11*, *25*) [and a modified version (*66*)] is in disagreement with several critical constraints. Most notably, the *β*-helix model does not fit within the unit cell packing dimensions of the EM data for which it was modeled. In addition, the *β*-helix model is inconsistent with

antibody mapping studies, enzyme cleavage sites and fibril disaggregation profiles, and the finding that main chain−main chain interactions are critical in aggregate formation. For a summary of all comparisons, see Table 2. Most importantly, evaluation of the models has allowed for seemingly disparate experimental constraints to be connected, resulting in an improved characterization of the properties of prion aggregates.

As our knowledge of the structural properties of prion protofibrils expands, so will our set of constraints. While we lack sufficient experimental constraints to determine the structure of prion protofibrils unambiguously, building a reasonable model can provide a target, and the impetus, for probing the structure of protein aggregates that have eluded conventional structure determination methods. While careful consideration of the two prevailing protofibril models indicates that the spiral model is a plausible protofibril model and that the β-helix is not, it does not rule out the possibility that there are other structures that would satisfy the experimental constraints. Indeed, given the heterogeneity of protofibrils and fibrils, we expect it.

ACKNOWLEDGMENT

We thank Dr. R. Stenkamp for helpful discussions and for sharing his XtalView expertise and Dr. C. Govaerts for providing coordinates of the β-helix model.

REFERENCES

1. Griffith, J. S. (1967) Self-Replication and scrapie, *Nature 215*, 1043−1044.
2. Prusiner, S. B. (1998) Prions, *Proc. Natl. Acad. Sci. U.S.A. 95*, 13363−13383.
3. Mouillet-Richard, S., Ermonval, M., Chebassier, C., Laplanche, J. L., Lehmann, S., Launay, J. M., and Kellermann, O. (2000) Signal transduction through prion protein, *Science 289*, 1925−1928.
4. Burns, C. S., Aronoff-Spencer, E., Dunham, C. M., Lario, P., Avdievich, N. I., Antholine, W. E., Olmstead, M. M., Vrielink, A., Gerfen, G. J., Peisach, J., Scott, W. G., and Millhauser, G. L. (2002) Molecular features of the copper binding sites in the octarepeat domain of the prion protein, *Biochemistry 41*, 3991−4001.
5. Borchelt, D. R., Scott, M., Taraboulos, A., Stahl, N., and Prusiner, S. B. (1990) Scrapie and cellular prion proteins differ in their kinetics of synthesis and topology in cultured-cells, *J. Cell Biol. 110*, 743−752.
6. Caughey, B., and Raymond, G. J. (1991) The scrapie-associated form of PrP is made from a cell-surface precursor that is both protease-sensitive and phospholipase-sensitive, *J. Biol. Chem. 266*, 18217−18223.
7. Caughey, B., Raymond, G. J., Ernst, D., and Race, R. E. (1991) N-Terminal truncation of the scrapie-associated form of PrP by lysosomal protease(s)—Implications regarding the site of conversion of PrP to the protease-resistant state, *J. Virol. 65*, 6597−6603.
8. Borchelt, D. R., Taraboulos, A., and Prusiner, S. B. (1992) Evidence for synthesis of scrapie prion proteins in the endocytic pathway, *J. Biol. Chem. 267*, 16188−16199.
9. Merz, P. A., Somerville, R. A., Wisniewski, H. M., and Iqbal, K. (1981) Abnormal fibrils from scrapie-infected brain, *Acta Neuropathol. (Berlin) 54*, 63−74.
10. Prusiner, S. B., Mckinley, M. P., Bowman, K. A., Bolton, D. C., Bendheim, P. E., Groth, D. F., and Glenner, G. G. (1983) Scrapie prions aggregate to form amyloid-like birefringent rods, *Cell 35*, 349−358.
11. Wille, H., Michelitsch, M. D., Guenebaut, V., Supattapone, S., Serban, A., Cohen, F. E., Agard, D. A., and Prusiner, S. B. (2002) Structural studies of the scrapie prion protein by electron crystallography, *Proc. Natl. Acad. Sci. U.S.A. 99*, 3563−3568.
12. Diringer, H., Gelderblom, H., Hilmert, H., Ozel, M., Edelbluth, C., and Kimberlin, R. H. (1983) Scrapie infectivity, fibrils and low-molecular weight protein, *Nature 306*, 476−478.
13. Meyer, R. K., Mckinley, M. P., Bowman, K. A., Braunfeld, M. B., Barry, R. A., and Prusiner, S. B. (1986) Separation and properties of cellular and scrapie prion proteins, *Proc. Natl. Acad. Sci. U.S.A. 83*, 2310−2314.
14. Caughey, B. W., Dong, A., Bhat, K. S., Ernst, D., Hayes, S. F., and Caughey, W. S. (1991) Secondary structure-analysis of the scrapie-associated protein PrP 27-30 in water by infrared-spectroscopy, *Biochemistry 30*, 7672−7680.
15. Pan, K. M., Baldwin, M., Nguyen, J., Gasset, M., Serban, A., Groth, D., Mehlhorn, I., Huang, Z. W., Fletterick, R. J., Cohen, F. E., and Prusiner, S. B. (1993) Conversion of α-helices into β-sheets features in the formation of the scrapie prion proteins, *Proc. Natl. Acad. Sci. U.S.A. 90*, 10962−10966.
16. Jackson, G. S., Hill, S. F., Joseph, C., Hosszu, L., Power, A., Waltho, J. P., Clarke, A. R., and Collinge, J. (1999) Multiple folding pathways for heterologously expressed human prion protein, *Biochim. Biophys. Acta 1431*, 1−13.
17. Hartley, D. M., Walsh, D. M., Ye, C. P. P., Diehl, T., Vasquez, S., Vassilev, P. M., Teplow, D. B., and Selkoe, D. J. (1999) Protofibrillar intermediates of amyloid beta-protein induce acute electrophysiological changes and progressive neurotoxicity in cortical neurons, *J. Neurosci. 19*, 8876−8884.
18. Bucciantini, M., Giannoni, E., Chiti, F., Baroni, F., Formigli, L., Zurdo, J. S., Taddei, N., Ramponi, G., Dobson, C. M., and Stefani, M. (2002) Inherent toxicity of aggregates implies a common mechanism for protein misfolding diseases, *Nature 416*, 507−511.
19. Kayed, R., Head, E., Thompson, J. L., McIntire, T. M., Milton, S. C., Cotman, C. W., and Glabe, C. G. (2003) Common structure of soluble amyloid oligomers implies common mechanism of pathogenesis, *Science 300*, 486−489.
20. Caughey, B., and Lansbury, P. T. (2003) Protofibrils, pores, fibrils, and neurodegeneration: Separating the responsible protein aggregates from the innocent bystanders, *Annu. Rev. Neurosci. 26*, 267−298.
21. Wille, H., Zhang, G. F., Baldwin, M. A., Cohen, F. E., and Prusiner, S. B. (1996) Separation of scrapie prion infectivity from PrP amyloid polymers, *J. Mol. Biol. 259*, 608−621.
22. Silveira, J. R., Raymond, G. J., Hughson, A. G., Race, R. E., Sim, V. L., Hayes, S. F., and Caughey, B. (2005) The most infectious prion protein particles, *Nature 437*, 257−261.
23. Saborio, G. P., Permanne, B., and Soto, C. (2001) Sensitive detection of pathological prion protein by cyclic amplification of protein misfolding, *Nature 411*, 810−813.
24. DeMarco, M. L., and Daggett, V. (2004) From conversion to aggregation: Protofibril formation of the prion protein, *Proc. Natl. Acad. Sci. U.S.A. 101*, 2293−2298.
25. Govaerts, C., Wille, H., Prusiner, S. B., and Cohen, F. E. (2004) Evidence for assembly of prions with left-handed β-helices into trimers, *Proc. Natl. Acad. Sci. U.S.A. 101*, 8342−8347.
26. Kostrewa, D., D'Arcy, A., Takacs, B., and Kamber, N. (2001) Crystal structures of *Streptococcus pneumoniae* N-acetylglucosamine-1-phosphate uridyltransferase, GlmU, in apo form at 2.33 Å resolution and in complex with UDP-N-acetylglucosamine and Mg^{2+} at 1.96 Å resolution, *J. Mol. Biol. 305*, 279−289.
27. Stimson, E., Hope, J., Chong, A., and Burlingame, A. L. (1999) Site-specific characterization of the N-linked glycans of murine prion protein by high-performance liquid chromatography electrospray mass spectrometry and exoglycosidase digestions, *Biochemistry 38*, 4885−4895.
28. Rudd, P. M., Endo, T., Colominas, C., Groth, D., Wheeler, S. F., Harvey, D. J., Wormald, M. R., Serban, H., Prusiner, S. B., Kobata, A., and Dwek, R. A. (1999) Glycosylation differences between the normal and pathogenic prion protein isoforms, *Proc. Natl. Acad. Sci. U.S.A. 96*, 13044−13049.
29. McRee, D. E. (1999) *Practical Protein Crystallography*, 2nd ed., p 477, Academic Press, San Diego, CA.
30. Alonso, D. O. V., DeArmond, S. J., Cohen, F. E., and Daggett, V. (2001) Mapping the early steps in the pH-induced conformational conversion of the prion protein, *Proc. Natl. Acad. Sci. U.S.A. 98*, 2985−2989.
31. Alonso, D. O. V., An, C., and Daggett, V. (2002) Simulations of biomolecules: characterization of the early steps in the pH-induced conformational conversion of the hamster, bovine and human forms of the prion protein, *Philos. Trans. R. Soc. London, Ser. B: Biol. Sci. 360*, 1165−1178.

32. DeMarco, M. L., and Daggett, V. (2005) Local environmental effects on the structure of the prion protein, *C. R. Biol. 328*, 847−862.
33. Leclerc, E., Peretz, D., Ball, H., Sakurai, H., Legname, G., Serban, A., Prusiner, S. B., Burton, D. R., and Williamson, R. A. (2001) Immobilized prion protein undergoes spontaneous rearrangement to a conformation having features in common with the infectious form, *EMBO J. 20*, 1547−1554.
34. Prusiner, S. B., Groth, D. F., Bolton, D. C., Kent, S. B., and Hood, L. E. (1984) Purification and structural studies of a major scrapie prion protein, *Cell 38*, 127−134.
35. Chiti, F., Webster, P., Taddei, N., Clark, A., Stefani, M., Ramponi, G., and Dobson, C. M. (1999) Designing conditions for in vitro formation of amyloid protofilaments and fibrils, *Proc. Natl. Acad. Sci. U.S.A. 96*, 3590−3594.
36. Chiti, F., Stefani, M., Taddei, N., Ramponi, G., and Dobson, C. M. (2003) Rationalization of the effects of mutations on peptide and protein aggregation rates, *Nature 424*, 805−808.
37. Makin, O. S., Atkins, E., Sikorski, P., Johansson, J., and Serpell, L. C. (2005) Molecular basis for amyloid fibril formation and stability, *Proc. Natl. Acad. Sci. U.S.A. 102*, 315−320.
38. Tracz, S. M., Abedini, A., Driscoll, M., and Raleigh, D. P. (2004) Role of aromatic interactions in amyloid formation by peptides derived from human amylin, *Biochemistry 43*, 15901−15908.
39. Blake, C., and Serpell, L. (1996) Synchrotron X-ray studies suggest that the core of the transthyretin amyloid fibril is a continuous β-sheet helix, *Structure 4*, 989−998.
40. Sunde, M., Serpell, L. C., Bartlam, M., Fraser, P. E., Pepys, M. B., and Blake, C. C. F. (1997) Common core structure of amyloid fibrils by synchrotron X-ray diffraction, *J. Mol. Biol. 273*, 729−739.
41. Fandrich, M., and Dobson, C. M. (2002) The behaviour of polyamino acids reveals an inverse side chain effect in amyloid structure formation, *EMBO J. 21*, 5682−5690.
42. Richardson, J. S., and Richardson, D. C. (2002) Natural β-sheet proteins use negative design to avoid edge-to-edge aggregation, *Proc. Natl. Acad. Sci. U.S.A. 99*, 2754−2759.
43. Nguyen, J. T., Inouye, H., Baldwin, M. A., Fletterick, R. J., Cohen, F. E., Prusiner, S. B., and Kirschner, D. A. (1995) X-ray diffraction of scrapie prion rods and PrP peptides, *J. Mol. Biol. 252*, 412−422.
44. Wang, J. M., Gulich, S., Bradford, C., Ramirez-Alvarodo, M., and Regan, L. (2005) A twisted four-sheeted model for an amyloid fibril, *Structure 13*, 1279−1288.
45. Nelson, R., Sawaya, M. R., Balbirnie, M., Madsen, A. O., Riekel, C., Grothe, R., and Eisenberg, D. (2005) Structure of the cross-β spine of amyloid-like fibrils, *Nature 435*, 773−778.
46. Hermann, L. M., and Caughey, B. (1998) The importance of the disulfide bond in prion protein conversion, *Neuroreport 9*, 2457−2461.
47. Welker, E., Raymond, L. D., Scheraga, H. A., and Caughey, B. (2002) Intramolecular versus intermolecular disulfide bonds in prion proteins, *J. Biol. Chem. 277*, 33477−33481.
48. Morrissey, M. P., and Shakhnovich, E. I. (1999) Evidence for the role of PrP^C helix 1 in the hydrophilic seeding of prion aggregates, *Proc. Natl. Acad. Sci. U.S.A. 96*, 11293−11298.
49. Ziegler, J., Viehrig, C., Geimer, S., Rosch, P., and Schwarzinger, S. (2006) Putative aggregation initiation sites in prion protein, *FEBS Lett. 580*, 2033−2040.
50. Ziegler, J., Sticht, H., Marx, U. C., Muller, W., Rosch, P., and Schwarzinger, S. (2003) CD and NMR studies of prion protein (PrP) helix 1. Novel implications for its role in the $PrP^C \rightarrow PrP^{Sc}$ conversion process, *J. Biol. Chem. 278*, 50175−50181.
51. Speare, J. O., Rush, T. S., III, Bloom, M. E., and Caughey, B. (2003) The role of helix 1 aspartates and salt bridges in the stability and conversion of prion protein, *J. Biol. Chem. 278*, 12522−12529.
52. Watzlawik, J., Skora, L., Frense, D., Griesinger, C., Zweckstetter, M., Schulz-Schaeffer, W. J., and Kramer, M. L. (2006) Prion protein helix 1 promotes aggregation but is not converted into β-sheet, *J. Biol. Chem.* (in press).
53. Novitskaya, V., Makarava, N., Bellon, A., Bocharova, O. V., Bronstein, I. B., Williamson, R. A., and Baskakov, I. V. (2006) Probing the conformation of the prion protein within a single amyloid fibril using a novel immunoconformational assay, *J. Biol. Chem. 281*, 15536−15545.
54. Chabry, J., Caughey, B., and Chesebro, B. (1998) Specific inhibition of in vitro formation of protease-resistant prion protein by synthetic peptides, *J. Biol. Chem. 273*, 13203−13207.
55. Lührs, T., Zahn, R., and Wüthrich, K. (2006) Amyloid formation by recombinant full-length prion proteins in phospholipid bicelle solutions, *J. Mol. Biol. 357*, 833−841.
56. Hope, J., Multhaup, G., Reekie, L. J., Kimberlin, R. H., and Beyreuther, K. (1988) Molecular pathology of scrapie-associated fibril protein (PrP) in mouse brain affected by the ME7 strain of scrapie, *Eur. J. Biochem. 172*, 271−277.
57. Glabe, C. G. (2004) Conformation-dependent antibodies target diseases of protein misfolding, *Trends Biochem. Sci. 29*, 542−547.
58. Peretz, D., Williamson, R. A., Kaneko, K., Vergara, J., Leclerc, E., Schmitt-Ulms, G., Mehlhorn, I. R., Legname, G., Wormald, M. R., Rudd, P. M., Dwek, R. A., Burton, D. R., and Prusiner, S. B. (2001) Antibodies inhibit prion propagation and clear cell cultures of prion infectivity, *Nature 412*, 739−743.
59. White, A. R., Enever, P., Tayebi, M., Mushens, R., Linehan, J., Brandner, S., Anstee, D., Collinge, J., and Hawke, S. (2003) Monoclonal antibodies inhibit prion replication and delay the development of prion disease, *Nature 422*, 80−83.
60. Williamson, R. A., Peretz, D., Pinilla, C., Ball, H., Bastidas, R. B., Rozenshteyn, R., Houghten, R. A., Prusiner, S. B., and Burton, D. R. (1998) Mapping the prion protein using recombinant antibodies, *J. Virol. 72*, 9413−9418.
61. Matucci, A., Zanusso, G., Gelati, M., Farinazzo, A., Fiorini, M., Ferrari, S., Andrighetto, G., Cestari, T., Caramelli, M., Negro, A., Morbin, M., Chiesa, R., Monaco, S., and Tridente, G. (2005) Analysis of mammalian scrapie protein by novel monoclonal antibodies recognizing distinct prion protein glycoforms: an immunoblot and immunohistochemical study at the light and electron microscopic levels, *Brain Res. Bull. 65*, 155−162.
62. Korth, C., Stierli, B., Streit, P., Moser, M., Schaller, O., Fischer, R., Schulz-Schaeffer, W., Kretzschmar, H., Raeber, A., Braun, U., Ehrensperger, F., Hornemann, S., Glockshuber, R., Riek, R., Billeter, M., Wüthrich, K., and Oesch, B. (1997) Prion (PrP^{Sc})-specific epitope defined by a monoclonal antibody, *Nature 390*, 74−77.
63. Horiuchi, M., Chabry, J., and Caughey, B. (1999) Specific binding of normal prion protein to the scrapie form via a localized domain initiates its conversion to the protease-resistant state, *EMBO J. 18*, 4085−4085.
64. Eghiaian, F., Grosclaude, J., Lesceu, S., Debey, P., Doublet, B., Treguer, E., Rezaei, H., and Knossow, M. (2004) Insight into the $PrP^C \rightarrow PrP^{Sc}$ conversion from the structures of antibody-bound ovine prion scrapie-susceptibility variants, *Proc. Natl. Acad. Sci. U.S.A. 101*, 10254−10259.
65. Paramithiotis, E., Pinard, M., Lawton, T., LaBoissiere, S., Leathers, V. L., Zou, W. Q., Estey, L. A., Lamontagne, J., Lehto, M. T., Kondejewski, L. H., Francoeur, G. P., Papadopoulos, M., Haghighat, A., Spatz, S. J., Head, M., Will, R., Ironside, J., O'Rourke, K., Tonelli, Q., Ledebur, H. C., Chakrabartty, A., and Cashman, N. R. (2003) A prion protein epitope selective for the pathologically misfolded conformation, *Nat. Med. 9*, 893−899.
66. Yang, S., Levine, H., Onuchic, J. N., and Cox, D. L. (2005) Structure of infectious prions: stabilization by domain swapping, *FASEB J. 19*, 1778−1782.
67. Daggett, V., and Levitt, M. (1992) Molecular-dynamics simulations of helix denaturation, *J. Mol. Biol. 223*, 1121−1138.

BI0612723